JOURNAL OF GEOPHYSICAL RESEARCH: ATMOSPHERES, VOL. 118, 8969–8983, doi:10.1002/jgrd.50693, 2013

Diagnostic analysis of interannual variation of global land evapotranspiration over 1982–2011: Assessing the impact of ENSO

Hao Yan,[1,2] Qin Yu,[2] Zai-Chun Zhu,[3] Ranga B. Myneni,[3] Hui-Min Yan,[4] Shao-Qiang Wang,[4] and Herman H. Shugart[2]

Received 3 December 2012; revised 13 July 2013; accepted 29 July 2013; published 29 August 2013.

[1] Global land evapotranspiration (E) between 1982 and 2011 was estimated by using a canopy conductance-based process E model (Air Relative Humidity-Based Two-Source model) [*Yan et al.*, 2012]. To analyze the impact of precipitation forcing on E, an ensemble of six E data sets was derived from a driving ensemble of six precipitation data sets (i.e., Global Historical Climatology Network, Global Precipitation Climatology Centre, Climate Research Unit, Global Dataset of Meteorological Forcings, Global Precipitation Climatology Project, and Delaware). The result shows that ensemble average E over global land had an annual mean of $64.8 \pm 0.8 \times 10^3$ km^3 yr^{-1} and a significant linear trend of 4.6 mm per decade ($p < 0.01$). Significant partial correlations were found between the ensemble average E and its three controlling variables (i.e., precipitation (P_r), vegetation leaf area index (L_{ai}), and potential evaporation (E_p)). These correlations explained 95% of the interannual variation of global land E with P_r as the dominant forcing contributing 37% variation of E; i.e., global land E was slightly sensitive to P_r than L_{ai} and E_p. P_r, L_{ai}, and E_p all showed increases of 8.8 mm ($p < 0.01$), 0.4 m^2 m^{-2} ($p < 0.01$), and 2.0 mm ($p < 0.1$) per decade, respectively, which characterized a favorable environment for the increase of E over past 30 years. Both negative Multivariate El Niño–Southern Oscillation (ENSO) Index (MEI) and Southern Oscillation Index (SOI) displayed an increasing trend. The La Niña phase tended to be dominant from 1982 to 2011 and caused a significant increase of land P_r and further enhanced land E. Impacts of ENSO and corresponding P_r variation require attention to increase the understanding of the interannual variation of global land E.

Citation: Yan, H., Q. Yu, Z.-C. Zhu, R. B. Myneni, H.-M. Yan, S.-Q. Wang, and H. H. Shugart (2013), Diagnostic analysis of interannual variation of global land evapotranspiration over 1982–2011: Assessing the impact of ENSO, *J. Geophys. Res. Atmos.*, *118*, 8969–8983, doi:10.1002/jgrd.50693.

1. Introduction

[2] Through biophysical processes including vegetation transpiration and soil evaporation, global land actual evapotranspiration (E) connects land surface water, energy, and carbon cycles and links the atmosphere to vegetation and soils in terrestrial ecosystems. As a key component in global land water cycle, E returns about 60% of annual land precipitation to the atmosphere [*Oki and Kanae*, 2006] and consumes more than half of absorbed solar energy [*Trenberth and Fasullo*, 2009].

[3] Knowledge of E is crucial to understanding how the water cycle has been impacted by climate change. Due to the lack of direct observations of land E at the global scale, many E models of varied complexity have been formulated based on different physical principles. These include surface conductance-based E models [*Leuning et al.*, 2008; *Mu et al.*, 2011; *Zhang et al.*, 2010; *Yan et al.*, 2012], energy-balance E models [*Su*, 2002; *Kustas and Norman*, 1999], coupled-stomata models for transpiration and photosynthesis [*Ryu et al.*, 2011; *Priestley and Taylor*, 1972], equation-based E model (GLEAM) [*Miralles et al.*, 2011b], and empirical E models [*Wang and Liang*, 2008; *Zeng et al.*, 2012; *Jung et al.*, 2010], such as the model tree ensemble approach (MTE) [*Jung et al.*, 2010] based on a set of explanatory variables (i.e., remote sensing data and surface meteorological data). These models have been evaluated with flux E data from subsets of the 400 available flux stations worldwide. Current estimation of global E from this suite of remote sensing-based models, as well as reanalysis (e.g., Modern Era Retrospective Analysis for Research and Applications

[1]National Meteorological Center, China Meteorological Administration, Beijing, China.
[2]Environmental Sciences Department, University of Virginia, Charlottesville, Virginia, USA.
[3]Department of Earth and Environment, Boston University, Boston, Massachusetts, USA.
[4]Institute of Geographic Sciences and Natural Resources Research, Chinese Academy of Sciences, Beijing, China.

Corresponding author: H. Yan, National Meteorological Center, China Meteorological Administration, #46 Zhongguancun South St., Haidian District, 100081 Beijing, China. (yanhaon@hotmail.com)

2169-897X/13/10.1002/jgrd.50693

(MERRA)) and off-line land surface models (e.g., Second Global Soil Wetness Project (GSWP-2)), ranges widely from 58×10^3 to $85 \times 10^3\,\mathrm{km^3\,yr^{-1}}$ by GSWP-2 [*Dirmeyer et al.*, 2006] and from 68×10^3 to $80 \times 10^3\,\mathrm{km^3\,yr^{-1}}$ by the LandFlux-EVAL project [*Mueller et al.*, 2011]. Along with these considerable differences, opposite trends in the change of the pattern of variation have been found in the period from 1984 to 2007 in different studies [e.g., *Jung et al.*, 2010; *Vinukollu et al.*, 2011]. Nevertheless, short-term analyses of global land E consistently show a decline from 1998 to 2008 [*Jung et al.*, 2010; *Vinukollu et al.*, 2011; *Zhang et al.*, 2010; *Zeng et al.*, 2012]. The first objective of the present study is to further examine E from 1998 up to 2011 to determine whether this decline continues.

[4] Intensification of global hydrologic cycle with warming temperatures has been confirmed based on evidence from precipitation and runoff data sets [*Huntington*, 2006; *Alkama et al.*, 2011]. Both climate models and satellite precipitation observations indicate that global (land and ocean) total atmospheric water, precipitation, and ocean evaporation have had similar, increasing trends (1.2 to 1.4% decade^{-1}) due to global temperature increase from 1987 to 2006 [*Wentz et al.*, 2007] and from the Pacific decadal variability as well [*Gu and Adler*, 2012]. However, intense and opposite precipitation anomalies can be seen over land and ocean due to El Niño–Southern Oscillation (ENSO) events [*Dai and Wigley*, 2000; *Trenberth et al.*, 2007].

[5] ENSO is regarded as the most important coupled ocean-atmosphere phenomenon causing climate (rainfall, temperature, vegetation, drought, flood, etc.) variability throughout the world on interannual time scales [*Dai et al.*, 1997; *Wolter and Timlin*, 1998]. Warm ENSO events (El Niño) tend to decrease global land precipitation [*Gu et al.*, 2007], but drought occurs during the warm El Niño and cold La Niña events of the ENSO phenomenon in different areas of the world [*Vicente-Serrano et al.*, 2011]. Reference evapotranspiration has a higher value up to 17%–30% in La Niña years than that in El Niño years in warm climates of Iran [*Sabziparvar et al.*, 2011] and in the Maipo River basin of Chile [*Meza*, 2005]. In addition, *Poveda et al.* [2001] pointed out that satellite normalized difference vegetation index (NDVI) exhibits strong negative anomalies during El Niño years in Colombia.

[6] Our second objective is to investigate whether ENSO events affect land E and contribute to the decline of E from 1998 to 2008 in addition to the soil moisture stress addressed by *Jung et al.* [2010]. Precipitation representing water supply E_p indicating atmosphere evaporation demand and vegetation L_{ai} showing canopy status are key drivers of E from the Penman-Monteith E model [*Monteith*, 1965]. Thus, ENSO-related precipitation anomalies should affect land E. However, the impact of ENSO on land E remains unknown except at small-river-basin scale [*Twine et al.*, 2005].

[7] The third objective in this study is to answer whether different precipitation data set affect the estimated trend of global land E. As global land E is more sensitive to P_r than net radiation perturbations [*Schlosser and Gao*, 2010] and uncertainty in P_r mostly translates to uncertainty in E [*Nasonova et al.*, 2011], it is essential to analyze the impact of ENSO-induced precipitation anomalies on interannual variation of land E. However, due to large uncertainties of current land precipitation data sets [*Mueller et al.*, 2013], precipitation trends should be interpreted with caution especially when deriving from a single precipitation data set [*Jung et al.*, 2010].

[8] To reduce the error of single P_r data set, we built an ensemble of P_r including six P_r member data sets that further produces six E ensemble members through Air Relative Humidity-Based Two-Source (ARTS) E model, which makes it possible to analyze the impact of P_r on E and finally give a reasonable estimation of ensemble average E with reduced error associated with input P_r of ensemble members. Thus, P_r uncertainty was mainly captured in this study while the rest of driving data sets came from a single reanalysis data set and not an ensemble.

[9] This study is the first long-term diagnostic analysis of the ENSO impact on global land E. An ensemble of global land E was generated at a monthly temporal scale and a 0.5° spatial scale for 1982–2011 using ARTS E model driven with six precipitation climate products and NASA MERRA reanalysis data. To provide a general picture of E variation associated with El Niño and La Niña events, interannual variation of E was analyzed against precipitation variation and two acceptable ENSO climate indices showing the strength of ENSO. Such knowledge will facilitate improved understanding of impact of global climate change on land water cycle.

2. Methods

[10] The Air Relative Humidity-Based Two-Source (ARTS) E model [*Yan et al.*, 2012] was adopted to estimate global land E. With assumption of no water stress, ARTS E model first calculates total E (E_0) as a sum of vegetation transpiration E_c and soil evaporation E_s. Similarly, the available energy A is partitioned into two parts: canopy part (A_c) and the soil part (A_s). Further correction of E_0 for soil water stress is conducted by using a soil water balance model. Evaluation against eddy covariance measurements at 19 flux sites, representing a wide variety of climate and vegetation types, indicated that monthly estimated E has an error statistics of root-mean-square error = 0.59 mm d^{-1}, bias = −0.05 mm d^{-1}, and R^2 = 0.77. These are values comparable to other E models [*Yan et al.*, 2012]. More detailed description of ARTS E model can be found in *Yan et al.* [2012].

2.1. Canopy Transpiration E_c and Canopy Conductance G_c

[11] The canopy transpiration (E_c) model is based on the Penman-Monteith model [*Monteith*, 1965], but the available energy (A) and surface conductance (G_s) terms are replaced by the canopy-absorbed available energy (A_c) and canopy conductance (G_c):

$$E_c = \frac{\Delta A_c + \rho C_p D G_a}{\Delta + \gamma\left(1 + G_a/G_c\right)}, \tag{1}$$

$$G_c = g_{s\max} \times R_h \times L_{ai}, \tag{2}$$

where A_c is the canopy available energy, Δ is the gradient of the saturated vapor pressure to air temperature, γ is the psychrometric constant, ρ is the density of air, C_p is the specific heat of air at constant pressure, G_a is the aerodynamic conductance, G_c is the canopy conductance accounting for transpiration from the vegetation, and $D = e_s - e_a$ is the vapor pressure deficit of the air, in which e_s is the saturation water vapor pressure at air temperature and e_a is the actual water vapor pressure, R_h is the air relative humidity, and g_{smax} is the maximum stomatal conductance assumed to have a value of 12.2 mm s^{-1} [*Kelliher et al.*, 1995].

2.2. Soil Evaporation E_s

[12] E_s equation is modified from the air relative humidity-based model of evapotranspiration (ARM-ET) [*Yan and Shugart*, 2010]:

$$E_s = 1.35 R_h \frac{\Delta A_s}{\Delta + \gamma}, \tag{3}$$

2.3. Total Evapotranspiration E_0 for Well-Watered Surface

[13] E_0 represents evapotranspiration for well-watered surface:

$$E_0 = \frac{\Delta A_c + \rho C_p D G_a}{\Delta + \gamma\left(1 + G_a/G_c\right)} + 1.35 R_h \frac{\Delta A_s}{\Delta + \gamma}. \tag{4}$$

2.4. Soil Water Correction Using Soil Water Balance Model

[14] As E_0 equals actual E only for a well-watered surface, a correction to E_0 is required for a water-stressed surface. Thus, a soil water balance model developed by *Thornthwaite and Mather* [1955] is adopted in ARTS E model to scale E_0 to actual E.

3. Data Sets and Preprocessing

3.1. MERRA Reanalysis Data

[15] Modern Era Retrospective Analysis for Research and Applications (MERRA) was developed by NASA using a major new version of the Goddard Earth Observing System Data Assimilation System Version 5 (GEOS-5), which focuses on historical analyses of the hydrological cycle aided by the NASA modern Earth Observing System (EOS) suite of satellite observations in a climate framework. MERRA produces temporally and spatially consistent analyses of atmosphere, land surface, and ocean surface variables at a spatial resolution of 0.5° latitude × 0.7° longitude from 1979 to present with significant improvements in precipitation and water vapor climatology [*Reichle et al.*, 2011; *Bosilovich et al.*, 2011]. It is ideal for investigating climate variability [*Rienecker et al.*, 2011].

3.2. Six Global Land Precipitation Data Sets

[16] The Global Historical Climatology Network (GHCN) monthly precipitation data set was created for climate monitoring at National Climatic Data Center (NCDC) of National Oceanic and Atmospheric Administration (NOAA). Monthly precipitation anomalies with respect to the 1961–1990 climate value were calculated from over 20,590 stations from 1900 to present. Station anomalies were then averaged within each 5° by 5° grid box to obtain the gridded GHCN precipitation product [*Peterson and Vose*, 1997; *Menne et al.*, 2012].

[17] The Global Precipitation Climatology Centre (GPCC), operated by National Meteorological Service of Germany under the auspices of the World Meteorological Organization (WMO), has generated a Full Data Reanalysis Product covering the period from 1901 to 2010 with a resolution of 0.5° by using an empirical interpolation method SPHEREMAP [*Willmott et al.*, 1985] from an available GPCC station database (67,200 stations with at least 10 years of data) compiled from all available sources [*Rudolf et al.*, 2011].

[18] The Climate Research Unit (CRU) at the University of East Anglia developed CRU 3.1 monthly climatic mean and time series of terrestrial surface climate for the period 1901–2009, which comprises seven climate elements (precipitation, mean temperature, diurnal temperature range, wet-day frequency, vapor pressure, cloud cover, and ground-frost frequency) [*New et al.*, 2000]. The spatial coverage extends over all land areas, excluding Antarctica. The construction method ensures that strict temporal fidelity is maintained. Monthly CRU time series data show month-by-month variations in climate variables and allow the comparison of variations in climate with variation in other phenomena [*New et al.*, 2000]. A 0.5° latitude/longitude gridded data set was adopted in this study.

[19] The Global Dataset of Meteorological Forcings (GDMP) was developed for land surface modeling by the Department of Civil and Environmental Engineering at the Princeton University. The data set includes precipitation, air temperature, surface pressure, specific humidity, wind speed, and downward long wave and short wave at surface and is currently available at a 1.0° monthly resolution for 1948–2008. It combines observations with the National Centers for Environmental Prediction–National Center for Atmospheric Research (NCEP-NCAR) reanalysis to correct known biases in the reanalysis precipitation and near-surface meteorology [*Sheffield et al.*, 2006].

[20] The Global Precipitation Climatology Project (GPCP) managed by NASA Goddard Space Flight Center was established by the World Climate Research Program (WCRP). It combines available satellite estimates including microwave estimates, infrared (IR) precipitation estimates, and additional low-Earth orbit estimates with monthly GPCC Precipitation Monitoring Product into a final merged product (V 2.2) covering global land and ocean at a 2.5° × 2.5° scale from 1979 to 2010 [*Huffman et al.*, 2009].

[21] The Delaware terrestrial precipitation monthly time series (V 3.01) was developed at the Department of Geography at the University of Delaware. Monthly total precipitation measured by rain gauge was compiled from several updated sources such as GHCN2 for the years 1900–2010 with the resultant number of stations ranging from about 4100 to 22,000 globally. Based on a relatively dense network of stations, a background precipitation climatology was built and was then interpolated to a 0.5° by 0.5° grid resolution with aid of monthly total precipitation by using climatologically aided interpolation method [*Willmott and Robeson*, 1995] to increase the accuracy of spatially interpolation.

3.3. Global Inventory Modeling and Mapping Studies (GIMMS) Leaf Area Index Data

[22] A new global 15 day LAI data set at 8 km spatial resolution for the period July 1981 to December 2011 was generated from advanced very high resolution radiometer

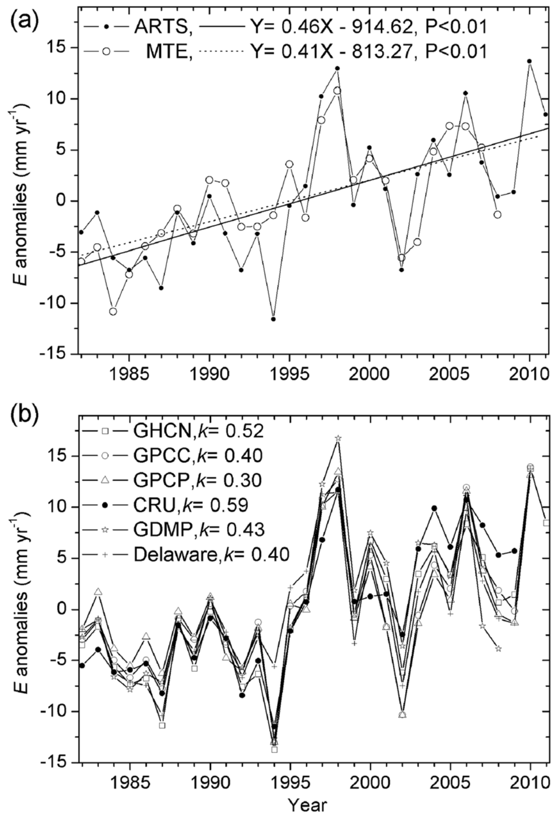

Figure 1. Interannual variation of (a) global land ARTS ensemble average E and (b) six ensemble members' E derived from respective driving precipitation data sets and corresponding slope k of linear trend from 1982 to 2011.

Global Inventory Modeling and Monitoring Study (GIMMS) NDVI3g data set using an Artificial Neural Network (ANN) model. The ANN model for generating the LAI data set was trained with overlapping GIMMS NDVI3g and best quality Moderate Resolution Imaging Spectroradiometer LAI data. The full temporal coverage GIMMS LAI3g data set was then generated using GIMMS NDVI3g data and the ANN model. The new GIMMS LAI3g data set was evaluated through direct comparison with field data and indirectly through (a) intercomparisons with similar satellite data products at biome and site scales, (b) testing for reproducing known relationships between LAI and climatic variables (temperature and precipitation), (c) canonical correlation analysis with ENSO/Arctic Oscillation indices, and (d) comparison to simulations from multiple dynamic vegetation models. These exercises resulted in establishing the validity and uncertainty of these new data sets. Further details can be found in *Zhu et al.* [2013].

3.4. ISLSCP II Global Gridded Soil Data

[23] Global 1° gridded surfaces of selected soil characteristics including maximum soil available water content (MAWC) for a soil depth of 0 ~ 150 cm was developed by the International Satellite Land Surface Climatology Project (ISLSCP) Initiative II project based on the International Geosphere-Biosphere Programme (IGBP)–Data and Information Services (DIS) soil data [*Global soil data task*, 2000].

3.5. GSWP-2 *E* Data

[24] The Second Global Soil Wetness Project (GSWP-2) as a recent environmental modeling research activity of the Global Land-Atmosphere System Study (GLASS) produced first global gridded multimodel analysis of land surface state variables and fluxes spanning 10 years (1986–1995) on a 0.5° grid and a monthly time scale. The resulting analysis consisting of multimodel means and standard deviations has been applied to studies of global terrestrial energy and water balance and major components of E [*Dirmeyer et al.*, 2006; *Dirmeyer*, 2011].

3.6. Multivariate ENSO Index (MEI) Data

[25] ENSO events and their strength have been monitored by using MEI index derived from six main observed variables over the tropical Pacific. These are sea level pressure, zonal and meridional components of the surface wind, sea surface temperature, surface air temperature, and total cloudiness fraction of the sky collected from the International Comprehensive Ocean-Atmosphere Data Set. Spatial filtering is initially applied to the individual fields and the first unrotated principal component (PC) of six filtered fields is regarded as MEI. Monthly MEI is computed for each of 12 sliding bimonthly periods (e.g., December/January, January/February). To keep the MEI comparable, all monthly MEI values are standardized based on a comparison with the 1950–1993 climate values [*Wolter and Timlin*, 1998].

3.7. Southern Oscillation Index (SOI) Data

[26] The SOI index also indicates the development and intensity of El Niño or La Niña events in the Pacific Ocean. It is a standardized anomaly of the mean sea level pressure difference between Tahiti and Darwin stations, which is usually calculated on a monthly basis at Australian Bureau of Meteorology. Further multiplication by 10 is their convention. Sustained negative values of the SOI greater than −8 often indicate El Niño episodes while sustained positive values of the SOI greater than +8 are typical of a La Niña episode [*Nicholls*, 1988].

3.8. Data Preprocessing

[27] All model forcings including six precipitation data sets, GIMMS L_{ai}, MERRA reanalysis meteorological data (i.e., net radiation, air temperature, specific humidity, wind speed, roughness length, and displacement height), and maximum soil available water content were resampled to a $0.5^o \times 0.5^o$ grid resolution by using a bilinear interpolation method and were then applied to driving the ARTS E model on a monthly time scale. GHCN P_r data sets only include anomalies and there is no available gridded GHCN P_r climate value. Thus, the CRU P_r climate value for the period 1961 to 1990 was instead added to GHCN P_r anomalies to build GHCN monthly P_r.

[28] To analyze interannual variation of E, monthly values of E were summed to yearly values and hence annual mean (equation (5)) and yearly bias (equation (6)) of E were calculated for six ensemble members, respectively. Further sum of averaged annual mean E and yearly bias E of six ensemble members produced a yearly series of ensemble average E over past 30 years (equation (7)),

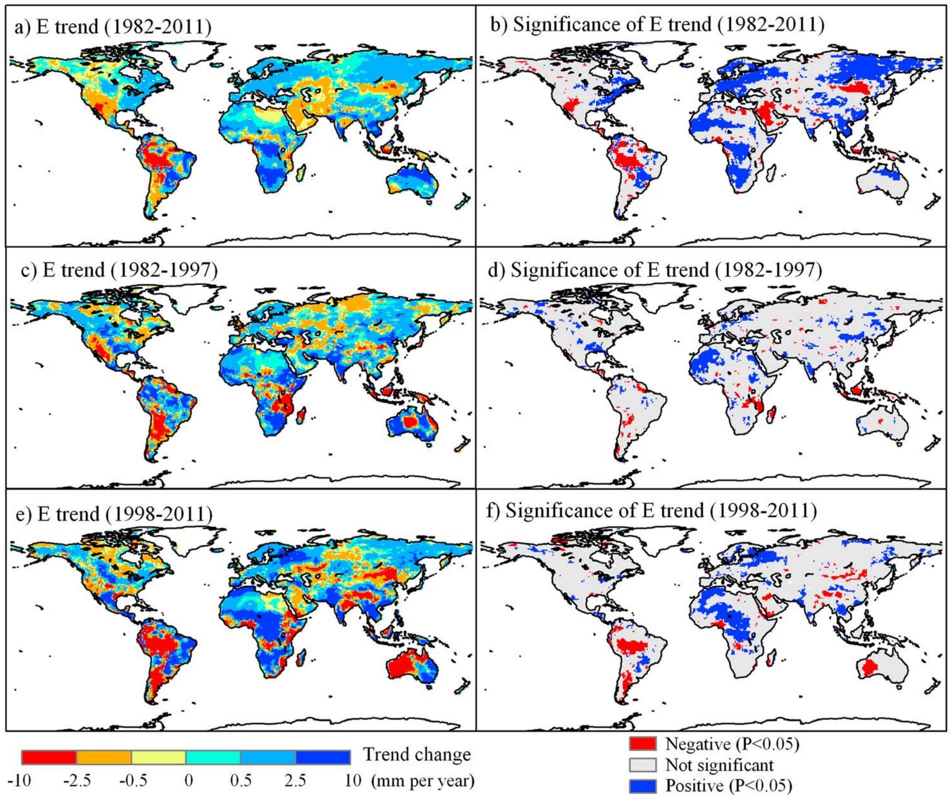

Figure 2. Distribution of global trend of ARTS ensemble average E and its significance of linear trend for period of (a, b) 1982–2011, (c, d) 1982–1997, and (e, f) 1998–2011, respectively.

which was then evaluated with GSWP-2 E data and previous studies:

$$E_{\mathrm{AnnualMean}} = \left(\sum_{\mathrm{Year}=1}^{N_y} \left(\sum_{\mathrm{Month}=1}^{12} E \right) \right) / N_y, \tag{5}$$

$$E_{\mathrm{YearlyBias}} = \left(\sum_{\mathrm{Month}=1}^{12} E \right) - E_{\mathrm{AnnualMean}}, \tag{6}$$

$$E_{\mathrm{EnsembleAverage}} = \left(\sum_{\mathrm{Member}=1}^{6} E_{\mathrm{AnnualMean}} \right) / 6 + \left(\sum_{\mathrm{Member}=1}^{N_m} E_{\mathrm{YearlyBias}} \right) / N_m, \tag{7}$$

where N_y is 30, 29, 28, 27, 29, and 29 years indicating the length of GHCN, GPCC, CRU, GDMP, GPCP, and Delaware P_r-derived E data sets, respectively. As a result, member number N_m is 1, 4, 5, and 6 for year 2011, 2010, 2009, and 1982 to 2008, respectively. Similarly, the ensemble of six precipitation data sets was processed.

[29] To analyze impact of atmosphere evaporation demand on E as a driving factor, E_p was calculated according to *Priestley and Taylor* [1972] (PT) equilibrium E model:

$$E_p = 1.26 \frac{\Delta A}{\Delta + \gamma}, \tag{8}$$

where variables have the same meanings to ARTS E model in section 2.2.

4. Results

4.1. Temporal and Spatial Variations of ARTS E

[30] The interannual variation of global ARTS ensemble average E from 1982 to 2011 (Figure 1a) clearly shows a significant increase with a trend of 0.46 mm yr^{-1} ($p < 0.01$), which coincides well with an increasing linear trend of 0.41 mm yr^{-1} ($p < 0.01$) given by MTE E model but for a shorter period of 1982–2008 [*Jung et al.*, 2010]. *Zeng et al*. [2012] reported a higher, also increasing rate of 1.1 ± 0.2 mm yr^{-1} ($p < 0.01$) for E from 1982 to 2009.

[31] E variation can be explicitly split into two periods (Figure 1a). During the first period (1982-1997), E had an increasing trend of 0.4 ($p = 0.14$) and 0.71 mm yr^{-1} ($p < 0.01$) indicated by ARTS and MTE models, respectively. Similarly, *Yan et al*. [2012], *Vinukollu et al*. [2011], and *Zeng et al*. [2012] reported an increasing trend of E over the 1980s and the 1990s. Whereas, during the second period (1998–2011) ARTS E shows no significant change due to two higher positive anomalies of 12.97 and 13.67 mm yr^{-1} occurred in the beginning (1998) and the end (2010) of the period, respectively (Figure 1a).

[32] However, a decreasing trend of 0.2 ($p = 0.66$) and 0.16 mm yr^{-1} ($p = 0.75$) was found over the interval of 1998–2008 by ARTS E and MTE E (Figure 1a). Earlier, *Jung et al*. [2010] based on an analysis of satellite microwave TRMM soil-moisture data found this trend and attributed it to limited moisture supply. However, the decreasing trend was not significant ($p > 0.60$) as shown here by both E models and other studies [*Vinukollu et al*., 2011; *Zeng et al*., 2012]. Thus, it can be regarded as a fluctuation accompanied with

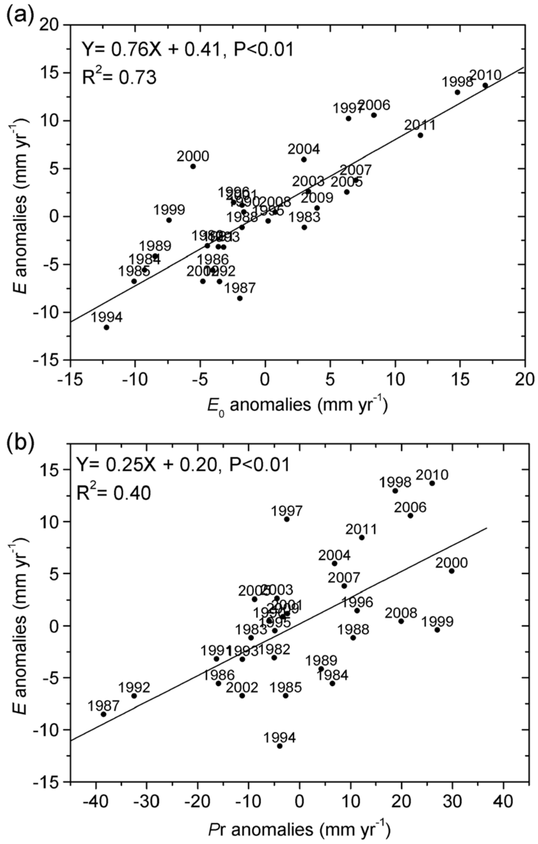

Figure 3. Scatterplot of anomalies of ensemble average (a) E versus E_0 and (b) E versus P_r.

a lower negative E anomaly of about $-6.0\,\mathrm{mm\,yr^{-1}}$ that occurred in 2002. Beyond this interval, ARTS E shows continued increase with a positive anomaly of $13.67\,\mathrm{mm\,yr^{-1}}$ in 2010. The decrease of E over 1998–2008 was temporary and does not reverse the increasing trend of E since 1982.

[33] Six E models, derived from respective P_r driving data set, all display similar interannual variation but different magnitude of anomalies (Figure 1b). Similar to the ARTS ensemble average E (Figure 1a), five E ensemble members had a significant increasing trend for the period of 1982–2011 ($p < 0.05$) except E_{GPCP} driven with GPCP P_r. The climatic trend of six E members ranged from $0.3\,\mathrm{mm\,yr^{-1}}$ for E_{GPCP} member to $0.59\,\mathrm{mm\,yr^{-1}}$ for E_{CRU} member. In addition, the increase from 1982 to 1997 and decrease from 1998 to 2011 of E were all insignificant for six ensemble members similar to ARTS ensemble average E (Figure 1a).

[34] With regard to spatial pattern of E for the whole research interval of 1982–2011 (Figures 2a and 2b), the ARTS ensemble average E had an overall increasing trend for most of the global land area while significant decreasing trend still existed in western North America, Amazon, Middle East, Northeast of China, etc. However, during the first period of 1982–1997, most land area shows an insignificant trend of E (Figures 2c and 2d). Conversely, during the second period of 1998–2011, more land areas (e.g., Australia and Amazon) had a decreasing trend of E while tropical Africa showed an increasing trend of E (Figures 2e and 2f).

4.2. Analysis of Driving Factors Resulting in the Intensified E

[35] In ARTS E model, E_0 represents total evapotranspiration under plentiful supply of water which is further scaled to actual E by using a soil water balance model. Thus, E_0 and P_r determine the actual E. On a global scale, both E_0 and ensemble average P_r had a close linear correlation ($p < 0.01$) with ARTS ensemble average E from 1982 to 2011, and furthermore, E_0 and P_r can explain 73% and 40% variation of E, respectively (Figure 3). In other words, global land E was predominantly controlled by E_0 rather than P_r. As E_0 actually included contributions of atmosphere demand and vegetation L_{ai} in ARTS E model, E_0 can substitute for E_p and L_{ai} as a comprehensive variable combined with P_r for analyzing impacts of model forcings on E.

[36] The interannual variations of global land P_r and E_0 from 1982 to 2011 (Figure 4) also show a significant increase with a trend of 0.88 ($p < 0.01$) and $0.51\,\mathrm{mm\,yr^{-1}}$ ($p < 0.01$), respectively, which produced an increasing trend of $E = 0.46\,\mathrm{mm\,yr^{-1}}$ ($p < 0.01$). Trends in E were consistent with increasing trends in P_r and E_0. *Jung et al.* [2010] also showed that P_r and E had consistent trends in research domain from 1998 to 2008. Figure 4 also indicates that the trend of E was lower than that of two driving factors, especially P_r, which might be due to that ecosystem had an reduced response to severe changes of P_r through its complex ecohydrological processes (e.g., soil water bank).

[37] The comparisons of anomalies of ensemble average P_r, E_0, and E (Figure 4) indicate that there probably existed a complementary relationship between E_0 and P_r in determining E on a global scale especially when anomalies of E_0 and P_r were large. For instance, annual precipitation was low in 1987 with a negative anomaly of $P_r = -38.46\,\mathrm{mm\,yr^{-1}}$, but E_0 only had a minor anomaly of $-1.94\,\mathrm{mm\,yr^{-1}}$, which resulted in an anomaly of $E = -8.52\,\mathrm{mm\,yr^{-1}}$, falling within anomalies of P_r and E_0. In another case with plentiful precipitation in 2000, even though E_0 had a negative anomaly of $-5.55\,\mathrm{mm\,yr^{-1}}$, the complementary effect due to plentiful precipitation with a positive anomaly of $P_r = 29.85\,\mathrm{mm\,yr^{-1}}$ produced an anomaly of $E = 5.23\,\mathrm{mm\,yr^{-1}}$. Note that E cannot exceed E_0 at any grid due to limitation by soil water balance model.

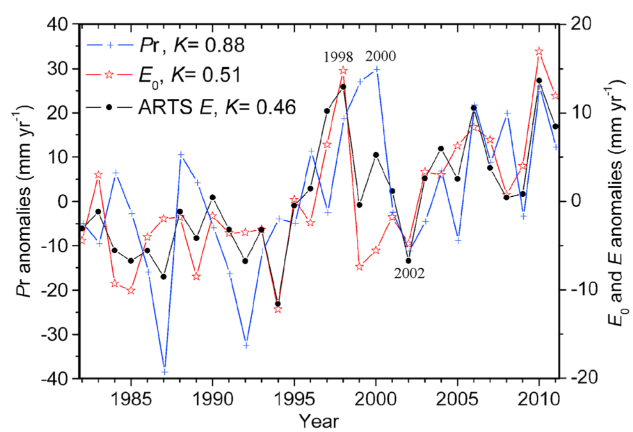

Figure 4. Interannual variations of global land E_0, ensemble average P_r and ARTS E from 1982 to 2011 and corresponding slope K of linear trend.

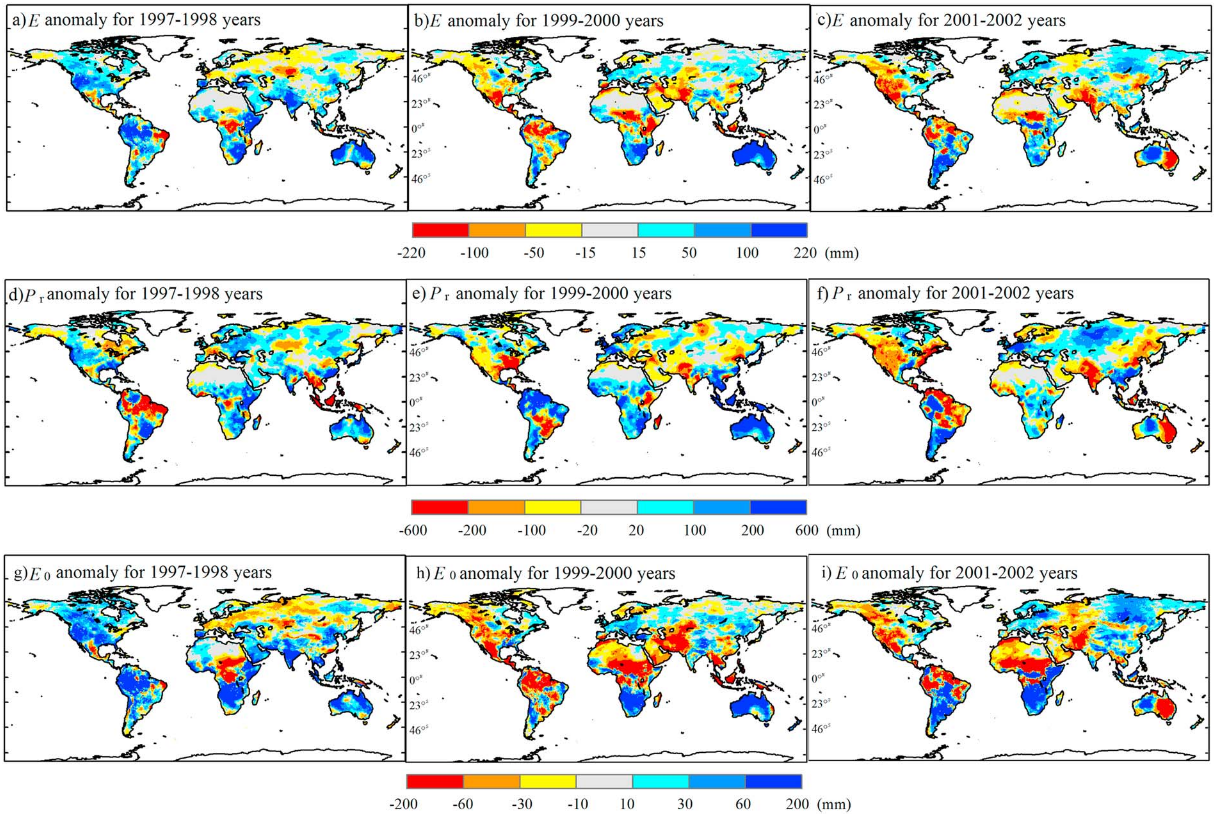

Figure 5. Pattern of (a–c) E, (d–f) P_r, and (g–i) E_0 anomalies for 1997–1998, 1999–2000, and 2001–2002.

[38] Figure 4 indicates that there were three sets of years of 1997–1998, 1999–2000, and 2001–2002 representing different combination of P_r, E_0, and E anomalies. The years 1997–1998 featured positive anomalies of annual mean P_r, E_0, and E; 1999–2000 had positive anomalies of P_r, negative anomalies of E_0, and a normal E while 2001–2002 featured negative anomalies of annual mean P_r, E_0, and E. Their spatial patterns show that there was plentiful P_r in tropical regions for 1999–2000 (Figure 5e) compared with 1997–1998 (Figure 5d). Conversely, E_0 shows an opposite pattern compared with P_r; there was less E_0, e.g., energy limitation, in tropical areas for 1999–2000 (Figure 5h) compared with 1997–1998 (Figure 5g). As a result of energy limitation, there was less E in tropical areas for 1999–2000 (Figure 5b) compared with 1997–1998 (Figure 5a), which indicates that those regions that were contributing more to the global land P_r anomalies were located in energy-limited regions (e.g., tropical regions in Figure 6e) and that is why there was not much P_r contribution to E during 1999–2000.

[39] In addition, 2001–2002 shows a different spatial pattern (Figures 5c, 5f, and 5i); P_r and E_0 had negative anomalies in more regions (Figures 5f and 5i) than those for 1997–1998. Thus, limited E_0 demand and P_r supply resulted in more regions with negative anomalies of E for 2001–2002 (Figure 5c) compared with 1997–1998 (Figure 5a).

[40] Figure 4 shows the comparisons of anomalies of E, E_0, and P_r globally. The complimentary relationship occurred in 21 years (70% of the years studied) and exceptions still existed in 9 years (30%), e.g., annual E needed not be a complimentary anomaly relative to P_r and E_0. For instance, P_r and E_0 all had a negative anomaly of -4.99 and $-4.44\ \mathrm{mm\,yr^{-1}}$ in 1982, respectively. This resulted in a weak negative anomaly of $E = -3.08\ \mathrm{mm\,yr^{-1}}$. Similarly, positive anomalies of $P_r = 26.0\ \mathrm{mm\,yr^{-1}}$ and $E_0 = 16.95\ \mathrm{mm\,yr^{-1}}$ in 2010 favored weak positive anomalies of $E = 13.67\ \mathrm{mm\,yr^{-1}}$. The above analysis further reveals that ecosystem tended to have a weak response of E with respect to dramatic changes of the two driving factors (i.e., P_r and E_0) on a global scale.

[41] The global variations of P_r, E_0, and E agreed with common knowledge that both favorable P_r and E_0 will produce a positive anomaly of E, or vice versa. In addition, complementary effects might reduce the amplitude of E anomaly when one factor had an opposite anomaly.

[42] To determine whether E_0 or P_r controls E as a major limitation factor, Pearson correlation coefficients of E versus E_0 and E versus P_r were calculated. Figures 6a and 6c shows that E was mainly determined by E_0 on global scale and P_r controlled E primarily in water-stressed areas such as deserts. Thus, E_0 was the major limitation factor of E over global land compared with P_r (Figure 6e). In contrast, it is well known that E_p often controlled E in tropical areas and Northern Hemisphere high-latitude areas (Figure 6b), which is consistent with *Wang et al.* [2010]. Thus, when conducting traditional forcing analysis by comparing E_p and P_r, one can derive a different map of major limiting factors (Figure 6f) that indicates more global land were controlled by P_r. There seems a paradox between Figures 6e and 6f. In fact, Figure 6f only considers the nonvegetation factors while Figure 6e reflects the impact of real vegetation on E by considering the canopy conductance; i.e., interannual

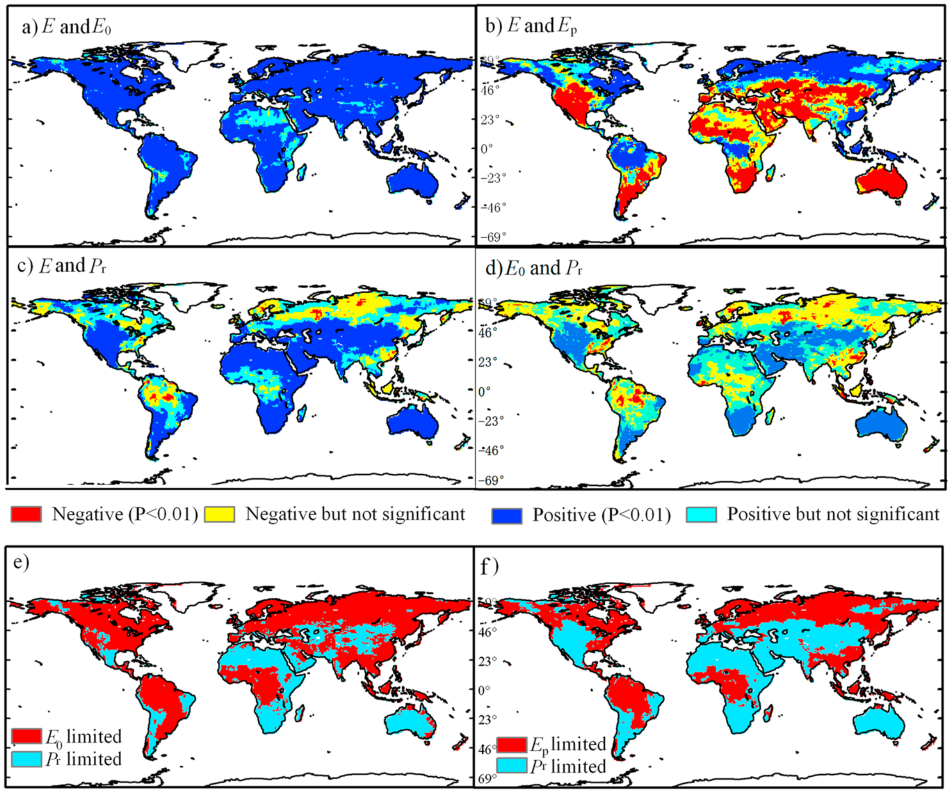

Figure 6. Pearson's correlation significance of (a) E versus E_0, (b) E versus PT E_p, (c) E versus P_r, and (d) E_0 versus P_r. (e) Map where E_0 demand or P_r supply limitation controls interannual variation of E. (f) Traditional map using E_p instead of E_0 as demand factor.

variation of E was principally controlled by canopy conductance-based E_0 in vegetation-covered land while in bare land, P_r controlled E through soil evaporation. In addition, intercorrelation analysis applied to E_0 and P_r (Figure 6d) shows that E_0 and P_r had negative relationships mainly in tropical areas and Northern Hemisphere high-latitude areas while significant positive relationships were often found in arid regions of southwest North America, southern South America, southern Africa, western Asia, and Australia.

[43] Global vegetation L_{ai} and MERRA T_a (Figure 7) had an increasing trend of $0.04\,m^2\,m^{-2}\,yr^{-1}$ ($p < 0.01$) and $0.024°C\,yr^{-1}$ ($p < 0.01$), respectively, while PT E_p had an increasing trend but insignificant in statistics ($p = 0.09$). Similarly, HadCRUT3 T_a data set shows a linear trend of $0.027°C\,yr^{-1}$ ($p < 0.01$) from 1979 to 2005 [*Brohan et al.*, 2006]. Global increase of L_{ai} (Figure 7) implied enhanced vegetation activity over the past three decades, which is consistent with previous studies of global greening since 1982 mainly because of improved critical climatic constraints to plant growth [*de Jong et al.*, 2012; *Nemani et al.*, 2003].

[44] ARTS ensemble average E had significant Pearson correlation with vegetation L_{ai} ($R^2 = 0.46$, $p < 0.01$), P_r ($R^2 = 0.40$, $p < 0.01$), and PT E_p ($R^2 = 0.22$, $p < 0.01$), respectively. From the view of vegetation regulation, water supply, and atmosphere demand that determined E, all driving factors, i.e., L_{ai}, P_r, and PT E_p, had an increasing trend in the 1982 to 2011 period (Figures 7 and 4). Thus, the recent increasing trend of global E can be primarily attributed to increasing vegetation L_{ai}, water supply, and atmosphere evaporation demand.

4.3. Uncertainties of Precipitation Variation and Its Impact on E

[45] Figure 8a shows that four P_r ensemble members (i.e., GHCN, GPCC, CRU, and GDMP) significantly increased by $0.87 \sim 1.53\,mm\,yr^{-1}$ for 1982–2011, while GPCP and Delaware P_r had an insignificant increase with a trend of 0.34 and $0.36\,mm\,yr^{-1}$ ($p > 0.05$), respectively. *Nickl et al.* [2010] reported an increased trend of P_r (at rates of approximately 0.75 to $2.1\,mm\,yr^{-1}$) over a decade from 1992 to 2002 estimated from GPCC, CRU, and Delaware P_r data sets. Figure 8a also implies that there existed large uncertainties in current P_r data sets. Six P_r ensemble members had a wide range of annual mean values from 99.2 ± 2.1 to $112.7 \pm 2.2 \times 10^3\,km^3\,yr^{-1}$ (Table 1).

[46] Comparison of standard deviation (STDEV) of ensemble average P_r and E calculated from corresponding six ensemble members (Figure 8b) indicates that ARTS E had an increasing trend of STDEV = $0.02\,mm\,yr^{-1}$ that was lower than that of P_r (trend of STDEV = $0.05\,mm\,yr^{-1}$), which have been seldom addressed by previous researches. As uncertainties of P_r, shown by the trend of STDEV for P_r, increased by $0.05\,mm\,yr^{-1}$ that was obviously lower than the increasing trend of $0.46\,mm\,yr^{-1}$ for ARTS ensemble average E, thus it can be concluded that uncertainties in P_r ensemble members could not substantially affect the increasing trend of global land E estimation.

4.4. Evaluation of ARTS Ensemble Average E

[47] We estimated an ensemble average E of $64.8 \pm 0.8 \times 10^3\,km^3\,yr^{-1}$, comparable to recent estimates of $65 \pm 3 \times 10^3$

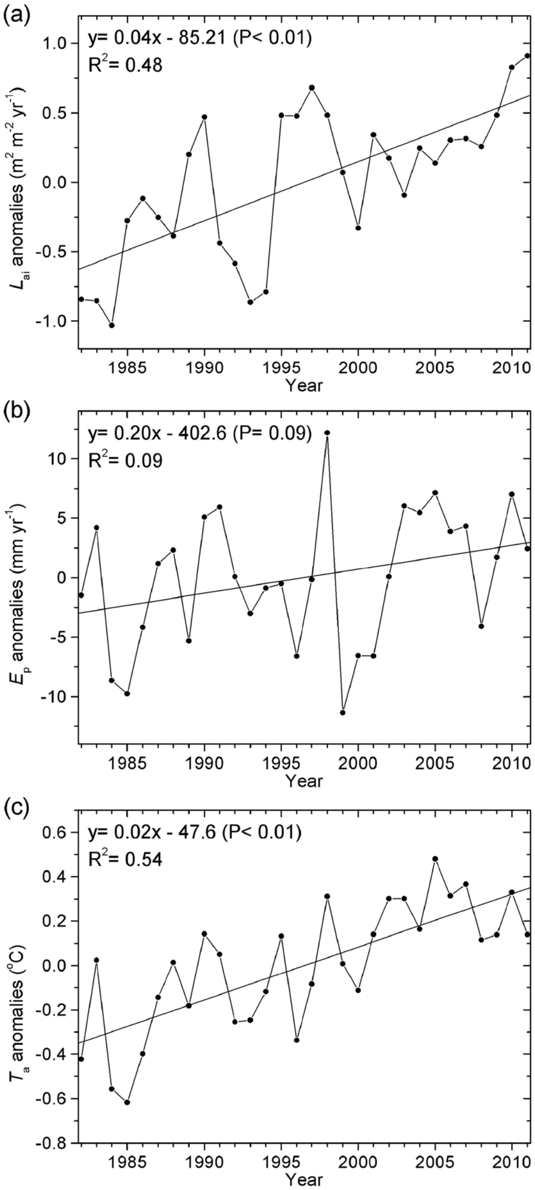

Figure 7. Interannual variations of global land (a) GIMMS L_{ai}, (b) PT E_p, and (c) T_a from 1982 to 2011.

[*Jung et al.*, 2010], 65.5×10^3 [*Oki and Kanae*, 2006], 62.8×10^3 [*Mu et al.*, 2011], 63×10^3 [*Ryu et al.*, 2011], 67×10^3 [*Trenberth et al.*, 2007], 69×10^3 [*Vinukollu et al.*, 2011], and $67.9 \times 10^3\,\mathrm{km}^3$ [*Miralles et al.*, 2011a]. *Schlosser and Gao* [2010] also reported a GSWP-2 model-mean value of $65.1 \pm 0.8 \times 10^3\,\mathrm{km}^3\,\mathrm{yr}^{-1}$ for global land excluding Antarctic.

[48] Six E ensemble members also had different annual E values with a narrow range of 63.7×10^3 to $68.3 \times 10^3\,\mathrm{km}^3\,\mathrm{yr}^{-1}$ (Table 1), which falls within the model range (49×10^3 to $82 \times 10^3\,\mathrm{km}^3\,\mathrm{yr}^{-1}$) estimated by the GSWP-2 project [*Schlosser and Gao*, 2010] and the recent model range (60×10^3 to $85 \times 10^3\,\mathrm{km}^3\,\mathrm{yr}^{-1}$) reported by the Water and Global Change project [*Haddeland et al.*, 2011]. As ensemble average P_r for global land was $102.8 \pm 2.1 \times 10^3\,\mathrm{km}^3\,\mathrm{yr}^{-1}$ (Table 1), the annual land E-to-P_r ratio was 0.63, which is close to reported values of 0.66 [*Dirmeyer*, 2011], 0.60 [*Zhang et al.*, 2010], and 0.58 ± 0.9 [*Alton et al.*, 2009]. ARTS ensemble average E (Figure 9) shows higher E over $1300\,\mathrm{mm\,yr}^{-1}$ mainly distributed in tropical American, African, and Asian areas due to plentiful supply of precipitation and heat. Whereas lower E less than $300\,\mathrm{mm\,yr}^{-1}$ often occurred in cold regions of Northern Hemisphere due to limited heat resources and in arid regions of Australia, Sahara, western and central Asia, etc., due to limited precipitation. Further comparison of ARTS E versus GSWP-2 E at grid scale (Figure 10) indicates a significant linear correlation ($p < 0.01$) with a slope $k = 0.98$. Significant correlation also existed on monthly comparisons (not shown). Above evaluations of ARTS ensemble average E show a reasonable spatial pattern of E.

5. Discussion and Conclusion

[49] According to the *Monteith* [1965] evaporation theory, land E is actually determined by water supply, atmosphere demand, and vegetation regulation that were expressed by P_r, E_p, and L_{ai}, respectively, in this study, and their effects on E was further analyzed to understand the increasing trend of E since 1982. Statistics of interannual variation indicate

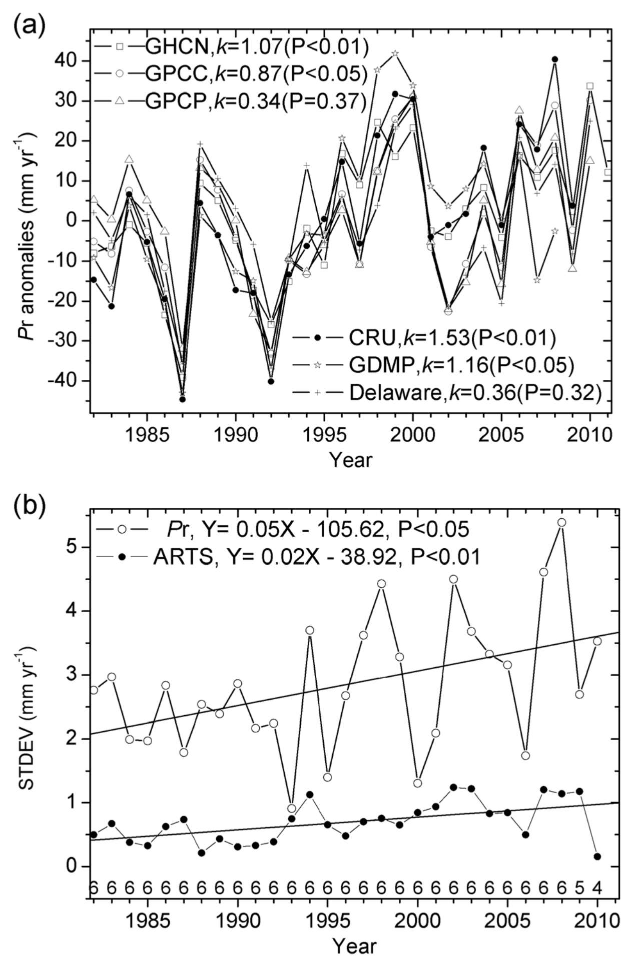

Figure 8. (a) Interannual variation of ensemble members' P_r for 1982–2011 and corresponding slope k and significance P of linear trend and (b) STDEV of ensemble average P_r and E calculated from ensemble members. Number of used ensemble members in a specific year is shown on top of x axis.

Table 1. Ensemble Average and STDEV of E and P_r and Associated Annual Mean of Six Ensemble Members for Global Land Excluding Antarctica and Greenland (Unit: $10^3\ km^3\ yr^{-1}$)

	Ensemble Average	GHCN	GPCC	GPCP	CRU	GDMP	Delaware
E	64.8 ± 0.8	65.3 ± 0.8	64.2 ± 0.8	68.3 ± 0.8	63.7 ± 0.8	64.6 ± 0.8	63.8 ± 0.8
P_r	102.8 ± 2.1	103.4 ± 2.1	103.7 ± 2.4	112.7 ± 2.2	101.1 ± 2.6	102.5 ± 2.6	99.2 ± 2.1

that significant Pearson correlations were found between E versus L_{ai}, P_r, and E_p with a determining coefficient R^2 of 0.46, 0.40, and 0.22, respectively, which shows that vegetation as the dominant forcing explained 46% variation of E. However, as the relationship between E and its three controlling variables is typical of multivariable correlation analysis and Pearson correlation fits better for bivariate analysis, thus partial correlation, due to its ability of measuring the degree of association between two random variables with the influence of the remaining variables eliminated, was adopted in this study. The result indicates significant partial correlations existed between E versus P_r, L_{ai}, and E_p with a determining coefficient R^2 of 0.37, 0.33, and 0.24, respectively; i.e., these three forcings explained 95% interannual variation of global land E in which E_p only contributed 24% variation of E while P_r contributed 37% variation of E. The statistics show that global land E was slightly more sensitive to P_r than other perturbations, which is consistent with the result of *Schlosser and Gao* [2010] and a feedback process described by *Dirmeyer et al*. [2009] that P_r very strongly determines soil moisture globally and hence soil moisture moderately controls land E.

[50] As water supply to E fundamentally comes from P_r and ENSO controls the interannual variation of global (land and ocean) P_r by shifting precipitation patterns in the tropics and subtropics due to changes of sea surface temperature in Pacific [*Trenberth*, 2011; *Curtis and Adler*, 2000], variation of global land P_r can be largely attributed to ENSO activities often characterized with ENSO climate index [*Gu and Adler*, 2011; *Dai and Wigley*, 2000; *Trenberth and Caron*, 2000]. Interannual variation of MEI and SOI (Figure 11a) indicates that −MEI and SOI significantly increased ($p < 0.05$) from 1982 to 2011; i.e., El Niño impact was weakening while La Niña impact was intensifying and hence resulting in more land P_r than normal, which was proved by the increasing trend of ensemble average P_r and a significant correlation between MEI and land P_r with $R^2 = 0.51$ ($p < 0.01$) shown in Figure 11a. As P_r acts as a controlling factor of the trend of E, thus it can be concluded that ENSO favored the increasing trend of global land E during the last 30 years, which has seldom been mentioned in previous studies.

[51] In addition, interannual variation of ensemble average P_r agreed to common knowledge that the global land annual P_r decreases significantly in El Niño years but increases evidently when La Niña events occur [*Gong and Wang*, 1999; *Mason and Goddard*, 2001; *Gu et al*., 2007]. However, ENSO indices did not agree well with P_r for the strongest ENSO event during 1997–2001 (Figure 11a), which may be due to the ENSO event itself undergoing long-period variations [*Gu et al*., 2007; *Vimont et al*., 2003]. Besides, volcanic eruptions such as the Mount Pinatubo in 1991 also caused an obvious drop in land precipitation accompanying a widespread drought [*Trenberth*, 2011; *Gu and Adler*, 2011].

[52] In addition, previous studies have illustrated the regional precipitation such as the Amazonia in South America is closely associated with the cycle of El Niño and La Niña. Long-term historical climate records of Amazonia in South America shows that the "average El Niño" is drier and warmer than normal in Amazonia, while the "average La Niña" is wetter and cooler [*Foley et al*., 2002]. Similarly, *Fu et al*. [2007] reported that the average annual precipitation is 494.8 mm in La Niña years and only 408.8 mm in El Niño years with a difference of 18.8% over the long-term average in the Yellow River basin of China.

[53] However, whether ENSO affects global land E is still not clear. We found that significant correlations existed between MEI and global land E excluding two outliers in 1997 and 1998 (Figure 11b) and between SOI and E (Figure 11c). We can get to a conclusion that ENSO could be a controlling factor of the interannual variability of E.

[54] We found that global land T_a and P_r all tended to increase since 1982 (Figures 7c and 8a), which seems to

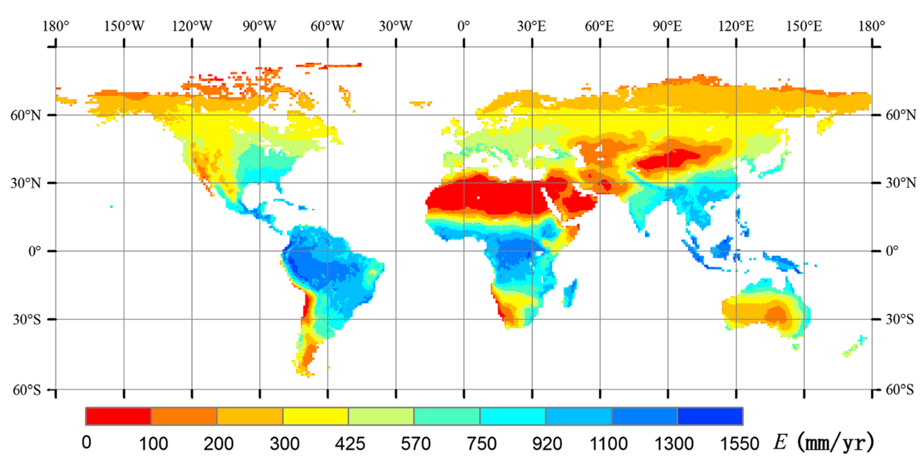

Figure 9. Spatial distribution of ARTS ensemble average E (1982–2011).

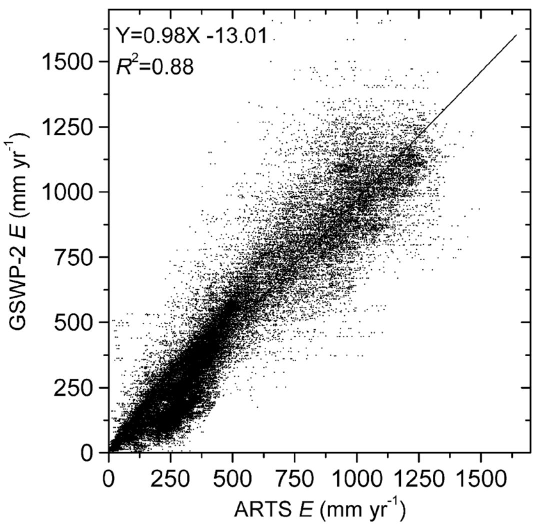

Figure 10. Comparison of ARTS ensemble E versus GSWP-2 E.

contradict the general concept of more P_r causing the decrease of T_a. In fact, *Trenberth and Fasullo* [2009] attribute the global warming to increasing absorbed solar radiation resulting from increasing greenhouse gases and water vapor that offsets, to a large degree, the increasing radiative emissions from global warming. Especially, water vapor in the air as the dominant greenhouse gas roughly doubles the T_a change due to its positive feedback effect [*Randall et al.*, 2007]. Thus, global warming does not necessarily correspond with a decline of land P_r. However, *Dai et al.* [2004] and *Trenberth* [2011] point out that higher temperatures have globally increased potential evapotranspiration and hence contribute to greater evaporation assuming no water stress. Similarly, increasing trend of PT E_p was found in this study mainly arising from higher temperatures (Figure 7).

[55] In addition, we found that there was a big change for MEI, P_r, E_0, and E from the first period of 1982–1997 to the second period of 1998–2011; P_r, E_0, and E all had a higher average value in the second period than that in the first period, which coincided with a negative average MEI = −0.05 in the second period of 1998-2011 featuring La Niña effect and a positive average MEI = 0.55 in the first period mainly suffering El Niño impact, respectively (Figure 11a). Similar studies show that 1997–1999 ENSO cycle was unique because during the transition from the warm 1997/1998 El Niño phase into the cold 1998/1999 La Niña phase, corresponding precipitation patterns were simultaneously strong and the 1997/1998 El Niño was the strongest event over last 20 years before 1999 [*Gong and Wang*, 1999; *Curtis and Adler*, 2000; *Curtis et al.*, 2001]. We found that in the transition year 1998 occurred the obvious positive anomaly of land $E = 12.97\ \mathrm{mm\,yr^{-1}}$. Recent 2009–2010 ENSO cycle also demonstrated a transition from the 2009–2010 El Niño phase to the 2010–2011 La Niña phase that resulted in the highest positive anomaly $E = 13.67\ \mathrm{mm\,yr^{-1}}$of 2010 during the last 30 years. It is our assessment that abnormal higher land E probably occurred during an obvious transition from El Niño phase to La Niña phase resulting in higher E_0 and P_r.

[56] According to the threshold of SOI = ±0.8 representing ENSO episode [*Nicholls*, 1988] and SOI time series over past 30 years (Figure 11a), typical El Niño years (i.e., 1987, 1992, 1994, and 2002) and La Niña years (i.e., 1999, 2000, 2010, and 2011) were selected. Further calculation of average anomalies of E, P_r, E_p and E_0 indicates a distinctive spatial pattern in El Niño and La Niña years, respectively. ENSO-induced land P_r anomaly (Figures 12c and 12d) had a spatial pattern consistent with previous results [*Dai and Wigley*, 2000; *Curtis and Adler*, 2003]. El Niño years (Figures 12a, 12c, 12e, and 12g) featured positive anomalies of E in southern South America, Mexico, and western Asia

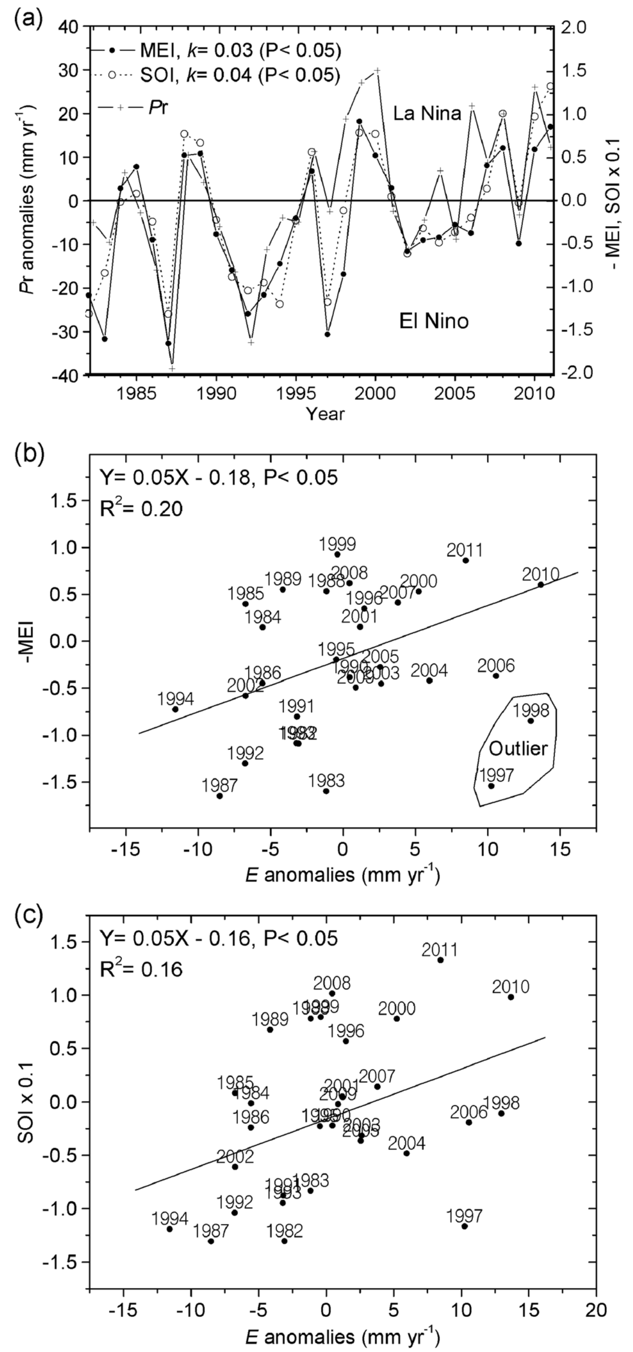

Figure 11. (a) Interannual variation of MEI multiplied by −1, SOI multiplied by 0.1, and global land P_r and scatterplot of anomalies of ensemble average (b) E versus −MEI and (c) E versus SOI × 0.1.

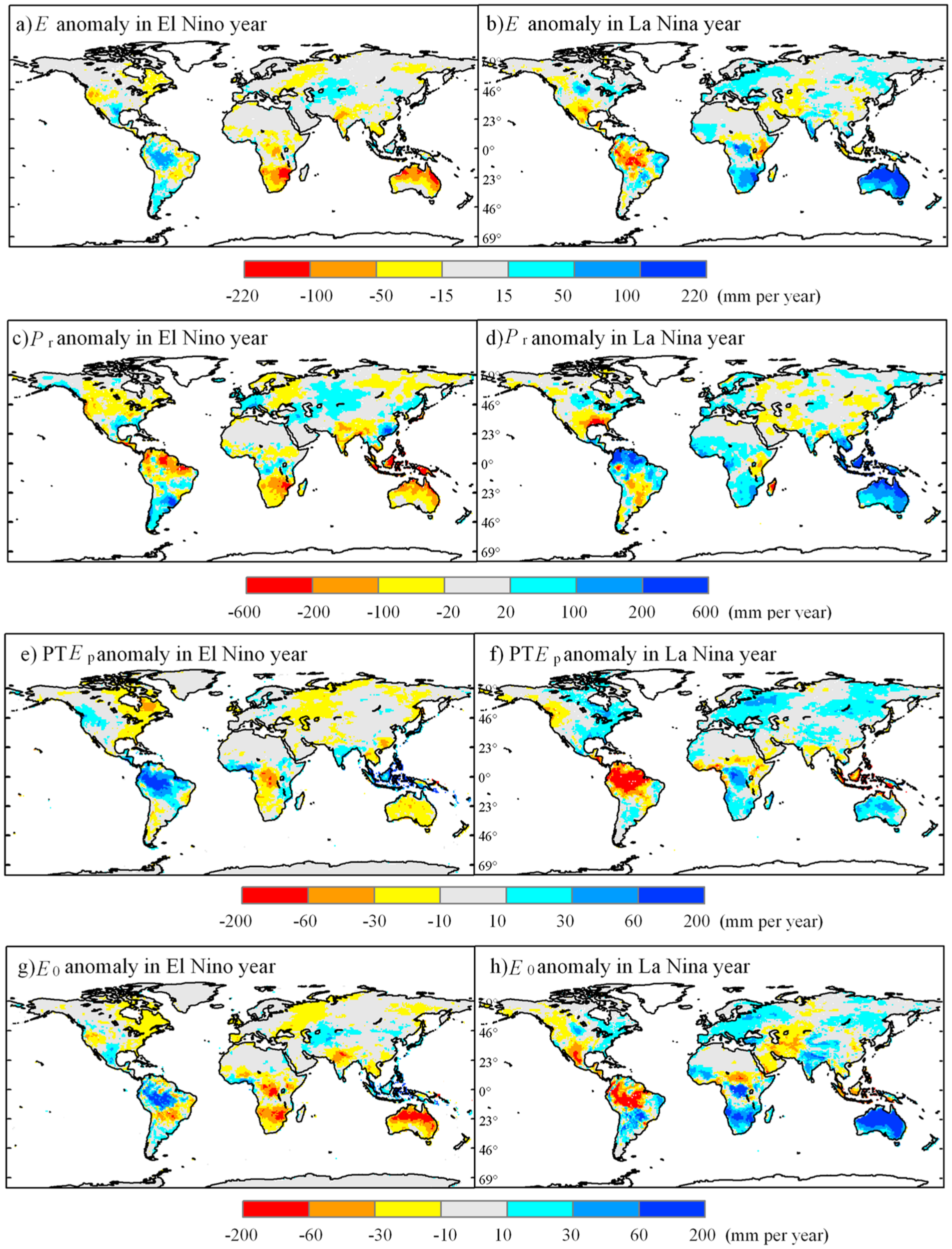

Figure 12. Pattern of (a, b) E, (c, d) P_r, (e, f) PT E_p, and (g, h) E_0 annual anomalies during El Niño and La Niña events.

because of more P_r while negative anomalies of E were found in Australia and southern Africa due to decreased P_r and E_p. These areas mainly suffered water supply limitation of P_r (Figure 12c). Although tropical Amazon and Asia islands experienced a decreased P_r in El Niño years, they still had a positive anomaly of E because El Niño-induced increase of E_p and E_0 satisfied its needs of heating resource. Conversely, tropical Africa rainforest had a decreasing E due to reduced E_p and E_0 (Figures 12e and 12g).

[57] However, La Niña years (Figures 12b, 12d, 12f, and 12h) indicate an almost reversed spatial pattern of E, P_r, E_p, and E_0 compared with that in El Niño years. For instance, Amazon experienced a negative anomaly of E resulting from a decreased E_p and E_0 while tropical Africa rainforest had an increasing E due to an enhanced E_p and E_0 (Figures 12f and 12h). Australia and southern Africa had positive anomalies of E mainly due to plentiful P_r plus increased E_p and E_0. In all, the response of E to ENSO events was essentially determined by whether its major limitation factor was E_p demand or P_r supply (Figures 6e and 6f). Besides, soil moisture memory affects E in some water-stressed areas as soil moisture memory can last up to a short period of 90 days [*Dirmeyer et al.*, 2009].

[58] *Jung et al.* [2010] initially reported the recent decline in the global land E trend from 1988 to 2008 due to limited soil moisture supply. However, as P_r has a strong correlation (99% significance) with soil moisture globally [*Dirmeyer et al.*, 2009], we focused on the impact of precipitation on the decline instead of soil moisture. Our modeled results first proved the decline in ensemble average E and P_r trend over

1988 to 2008, but we found the decline was not only due to limited water supply of P_r but also due to decreased E_0 (Figure 4). In fact, E_0 reached its summit in 1998 corresponding with strong El Niño while P_r reached its summit in 1999/2000 associated with strong La Niña; then both E_0 and P_r kept decreasing until 2009, which jointly produced the decline of E (Figure 4). Note that E_0 represents E assuming no water stress under current vegetation and atmosphere conditions.

[59] In addition, the decline was fundamentally due to natural climate variability of ENSO (Figure 11a); The longest 1999–2000 La Niña event since 1982 gave a higher positive anomaly of $P_r = 26.1\ \mathrm{mm\,yr^{-1}}$ and the following La Niña event that occurred in 2007–2009 brought a lower positive anomaly of $P_r = 10.2\ \mathrm{mm\,yr^{-1}}$. Between these two La Niña events were several El Niño events featuring weak land precipitation, i.e., ENSO-induced decreasing of P_r resulted in the limited water supply and hence the decline of E from 1988 to 2008. Thus, ENSO was the fundamental reason for the decline of E while P_r and soil moisture featuring limited water supply were the direct reason, which answers the concern of *Jung et al*. [2010] whether the decline of E is representative of natural climate variability.

[60] Furthermore, *Jung et al*. [2010] argued whether the decline of E is permanent indicating reorganization of the land water cycle. We found that decline of E was temporary because E continued to increase to another summit in 2010 (Figure 1a) and MEI, P_r, E_0, and E all featured an enhanced land water cycle during the period of 1998–2011 compared with the first period of 1982–1997. Variation of P_r indicates wetter climate in 2010 and 2011 (Figure 4) consistent with climate analysis based on GHCN and GPCC precipitation record [*Blunden and Arndt*, 2012].

[61] Fundamentally, ENSO is the largest signal in the interannual variation of ocean-atmosphere system [*Wang et al*., 1999]. It originates from the tropical Pacific but affects the global climate through teleconnection effect via changes in the circulation patterns. Numerous studies have identified ENSO-induced climate variability of precipitation, temperature, reference evapotranspiration, water balance, and drought [*Yang and DelSole*, 2011; *Ropelewski and Halpert*, 1986; *Meza*, 2005; *Twine et al*., 2005; *Coelho and Goddard*, 2009]. Besides, we found that ENSO impacted the interannual variation of global land E through the similar mechanism of teleconnection.

[62] Currently, large difference still exists among global estimations of E given by different studies [*Jung et al*., 2010; *Trenberth et al*., 2007; *Vinukollu et al*., 2011; *Miralles et al*., 2011a] because of uncertain forcing and model mechanism [*Schlosser and Gao*, 2010; *Yan et al*., 2012]. As the model range of global E estimates is larger than any bias caused by uncertainties in the model forcings [*Vinukollu et al*., 2011; *Schlosser and Gao*, 2010], model mechanism should be improved with first priority. For example, the E models, due to using air humidity as a surrogate to soil moisture, may not reflect the decline in E in the 2000s due to soil moisture limitation that mainly occurred in the Southern Hemisphere [*Vinukollu et al*., 2011]. ARTS E model as a revised Penman-Monteith model [*Monteith*, 1965] explicitly considers canopy conductance derived from remote sensing L_{ai}, energy balance and water balance [*Yan et al*., 2012]. Although ARTS E model considers the snow melting effect, snow sublimation effect will be studied in our future work because snow sublimation, dominating E in high latitudes in winter and in the mountainous regions of midlatitudes, occupies 2% of global land E [*Miralles et al*., 2011b].

[63] However, *Jiménez et al*. [2011] argued that whether model forcing adds less uncertainty than E different parameterizations depends on what processes are analyzed and over what regions. Thus, there are currently international efforts trying to get a better understanding of the whole E estimation, such as the Global Energy and Water Cycle Experiment coordinated evaluation of E estimates by the LandFlux-EVAL initiative [*Jiménez et al*., 2011; *Mueller et al*., 2011].

[64] As water balance was actually driven by P_r data in ARTS E model and different P_r products had some differences (Figure 8a) and even different spatial pattern of trends (not shown) due to different numbers of observing stations [*Blunden and Arndt*, 2012], different interpolation method [*Willmott and Robeson*, 1995], and merging of satellite precipitation production in GPCP [*Huffman et al*., 2009], we adopted the ensemble method to obtain ensemble average P_r and E to reduce the impact of input error of P_r. The ensemble average P_r had an increasing trend consistent with precipitation climate analysis by *Blunden and Arndt* [2012].

[65] Similarly, large differences found in radiation dada affect global estimation of E [*Vinukollu et al*., 2011; *Yan et al*., 2012]. Two satellite radiation products, i.e., International Satellite Cloud Climatology Project and Surface Radiation Budget (SRB) radiation products, show temporal inconsistencies due to changes in satellite sensors and retrieval algorithms [*Vinukollu et al*., 2011]. In addition, the negative bias of SRB net radiation partly resulted in a lower global E estimate of $58.4 \times 10^3\ \mathrm{km^3\,yr^{-1}}$ [*Yan et al*., 2012]. However, as interannual variation of global E was more sensitive to P_r and L_{ai} than E_p perturbations already reflecting the impact of net radiation, uncertainties in radiation data of MERRA reanalysis cannot substantially affect the main conclusions of this study.

[66] To reduce uncertainty in E estimates, improving model and forcing continues to be essential [*Mueller et al*., 2011; *Vinukollu et al*., 2011; *Yan et al*., 2012]. For example, GLEAM E model [*Miralles et al*., 2011b] considers more processes including the rainfall interception and snow sublimation and incorporates Advanced Microwave Scanning Radiometer–EOS microwave-derived land surface temperature, vegetation optical depth to capture vegetation phenology [*Jones et al*., 2011], and soil moisture which may result in a better representation of the water supply process as well as evaporation stress.

[67] However, it is our assessment that to build ensemble average E, based on ensemble of forcing data and E models, was an available method to obtain a reasonable estimation of global land E with deviation statistics. This study preliminarily built an ensemble of six precipitation data sets and then analyzed an ensemble of six independent E products estimated from one single ARTS E model over the period of 1982 to 2011. Further ensemble analysis of more E models and forcings including radiation will be conducted in the next step of work.

[68] **Acknowledgments.** This work was supported by National Natural Science Foundation of China (41171284, 40801129), Chinese Academy of Sciences (XDA05050602-1), and China Scholarship Council Foundation and partly funded by NASA Earth Science Division, as well as by the following NASA grants to H.H. Shugart: 10-CARBON10-0068 and Climate Change/09-IDS09-116. The reviewers are thanked for their constructive remarks and suggestions.

References

Alkama, R., B. Decharme, H. Douville, and A. Ribes (2011), Trends in global and basin-scale runoff over the late twentieth century: Methodological issues and sources of uncertainty, *J. Climate*, *24*(12), 3,000–3,014.

Alton, P., R. Fisher, S. Los, and M. Williams (2009), Simulations of global evapotranspiration using semiempirical and mechanistic schemes of plant hydrology, *Global Biogeochem. Cycles*, *23*, GB4023, doi:10.1029/2009GB003540.

Blunden, J., and D. S. Arndt (2012), State of the climate in 2011, *Bull. Am. Meteorol. Soc.*, *93*(7), S1–S282.

Bosilovich, M. G., F. R. Robertson, and J. Chen (2011), Global energy and water budgets in MERRA, *J. Climate*, *24*(22), 5,721–5,739.

Brohan, P., J. J. Kennedy, I. Harris, S. F. B. Tett, and P. D. Jones (2006), Uncertainty estimates in regional and global observed temperature changes: A new data set from 1850, *J. Geophys. Res.*, *111*, D12106, doi:10.1029/2005JD006548.

Coelho, C. A. S., and L. Goddard (2009), El Niño-induced tropical droughts in climate change projections, *J. Climate*, *22*(23), 6,456–6,476.

Curtis, S., and R. Adler (2000), ENSO indices based on patterns of satellite-derived precipitation, *J. Climate*, *13*(15), 2,786–2,793.

Curtis, S., and R. F. Adler (2003), Evolution of El Niño-precipitation relationships from satellites and gauges, *J. Geophys. Res.*, *108*(D4), 4153, doi:10.1029/2002JD002690.

Curtis, S., R. Adler, G. Huffman, E. Nelkin, and D. Bolvin (2001), Evolution of tropical and extratropical precipitation anomalies during the 1997–1999 ENSO cycle, *Int. J. Climatol.*, *21*(8), 961–971.

Dai, A., and T. M. L. Wigley (2000), Global patterns of ENSO induced precipitation, *Geophys. Res. Lett.*, *27*(9), 1,283–1,286.

Dai, A., I. Y. Fung, and A. D. DelGenio (1997), Surface observed global land precipitation variations during 1900–88, *J. Climate*, *10*(11), 2,943–2,962.

Dai, A., K. E. Trenberth, and T. Qian (2004), A global dataset of Palmer Drought Severity Index for 1870–2002: Relationship with soil moisture and effects of surface warming, *J. Hydrometeorol.*, *5*(6), 1,117–1,130.

Dirmeyer, P. A. (2011), A history and review of the Global Soil Wetness Project (GSWP), *J. Hydrometeorol.*, *12*(5), 729–749.

Dirmeyer, P. A., X. Gao, M. Zhao, Z. Guo, T. Oki, and N. Hanasaki (2006), GSWP-2: Multimodel analysis and implications for our perception of the land surface, *Bull. Am. Meteorol. Soc.*, *87*(10), 1,381–1,397.

Dirmeyer, P. A., C. A. Schlosser, and K. L. Brubaker (2009), Precipitation, recycling, and land memory: An integrated analysis, *J. Hydrometeorol.*, *10*(1), 278–288.

Foley, J. A., A. Botta, M. T. Coe, and M. H. Costa (2002), El Niño–Southern Oscillation and the climate, ecosystems and rivers of Amazonia, *Global Biogeochem. Cycles*, *16*(4), 1132, doi:10.1029/2002GB001872.

Fu, G., S. P. Charles, N. R. Viney, S. Chen, and J. Q. Wu (2007), Impacts of climate variability on stream-flow in the Yellow River, *Hydrol. Process*, *21*(25), 3,431–3,439.

Global Soil Data Task (2000), Global gridded surfaces of selected soil characteristics (IGBPDIS). International Geosphere-Biosphere Programme–Data and Information Services, Available online [http://www.daac.ornl.gov/] from the ORNL Distributed Active Archive Center, Oak Ridge National Laboratory, Oak Ridge, Tennessee, U.S.A.

Gong, D., and S. Wang (1999), Impacts of ENSO on rainfall of global land and China, *Chinese Sci. Bul.*, *44*(9), 852–856.

Gu, G., and R. F. Adler (2011), Precipitation and temperature variations on the interannual time scale: Assessing the impact of ENSO and volcanic eruptions, *J. Climate*, *24*(9), 2,258–2,270.

Gu, G., and R. Adler (2012), Interdecadal variability/long-term changes in global precipitation patterns during the past three decades: Global warming and/or Pacific decadal variability?, *Clim. Dyn.*, *1–14*.

Gu, G., R. F. Adler, G. J. Huffman, and S. Curtis (2007), Tropical rainfall variability on interannual-to-interdecadal and longer time scales derived from the GPCP monthly product, *J. Climate*, *20*(15), 4,033–4,046.

Haddeland, I., et al. (2011), Multimodel estimate of the global terrestrial water balance: Setup and first results, *J. Hydrometeorol.*, *12*(5), 869–884.

Huffman, G. J., R. F. Adler, D. T. Bolvin, and G. Gu (2009), Improving the global precipitation record: GPCP version 2.1, *Geophys. Res. Lett.*, *36*, L17808, doi:10.1029/2009GL040000.

Huntington, T. G. (2006), Evidence for intensification of the global water cycle: Review and synthesis, *J. Hydrol.*, *319*(1-4), 83–95.

Jiménez, C., et al. (2011), Global intercomparison of 12 land surface heat flux estimates, *J. Geophys. Res.*, *116*, D02102, doi:10.1029/2010JD014545.

Jones, M. O., L. A. Jones, J. S. Kimball, and K. C. McDonald (2011), Satellite passive microwave remote sensing for monitoring global land surface phenology, *Remote Sens. Environ.*, *115*(4), 1,102–1,114.

de Jong, R., J. Verbesselt, M. E. Schaepman, and S. de Bruin (2012), Trend changes in global greening and browning: Contribution of short-term trends to longer-term change, *Global Change Biol.*, *18*(2), 642–655.

Jung, M., et al. (2010), Recent decline in the global land evapotranspiration trend due to limited moisture supply, *Nature*, *467*(7318), 951–954.

Kelliher, F. M., R. Leuning, M. R. Raupach, and E. D. Schulze (1995), Maximum conductances for evaporation from global vegetation types, *Agr. Forest. Meteorol.*, *73*(1-2), 1–16.

Kustas, W. P., and J. M. Norman (1999), Evaluation of soil and vegetation heat flux predictions using a simple two-source model with radiometric temperatures for partial canopy cover, *Agr. Forest. Meteorol.*, *94*(1), 13–29.

Leuning, R., Y. Q. Zhang, A. Rajaud, H. Cleugh, and K. Tu (2008), A simple surface conductance model to estimate regional evaporation using MODIS leaf area index and the Penman-Monteith equation, *Water Resour. Res.*, *44*, W10419, doi:10.1029/2007WR006562.

Mason, S. J., and L. Goddard (2001), Probabilistic precipitation anomalies associated with ENSO, *Bull. Am. Meteorol. Soc.*, *82*(4), 619–638.

Menne, M. J., I. Durre, R. S. Vose, B. E. Gleason, and T. G. Houston (2012), An overview of the Global Historical Climatology Network-daily database, *J. Atmos. Oceanic Tech.*, *29*(7), 897–910.

Meza, F. J. (2005), Variability of reference evapotranspiration and water demands. Association to ENSO in the Maipo River basin, Chile, *Glob. Planet. Chang.*, *47*(2-4), 212–220.

Miralles, D. G., R. A. M. De Jeu, J. H. Gash, T. R. H. Holmes, and A. J. Dolman (2011a), Magnitude and variability of land evaporation and its components at the global scale, *Hydrol. Earth Syst. Sci.*, *15*(3), 967–981.

Miralles, D. G., T. R. H. Holmes, R. A. M. De Jeu, J. H. Gash, A. G. C. A. Meesters, and A. J. Dolman (2011b), Global land-surface evaporation estimated from satellite-based observations, *Hydrol. Earth Syst. Sci.*, *15*(2), 453–469.

Monteith, J. L. (1965), Evaporation and the environment, *Symp. Soc. Exp. Biol.*, *19*, 205–234.

Mu, Q., M. Zhao, and S. W. Running (2011), Improvements to a MODIS global terrestrial evapotranspiration algorithm, *Remote Sens. Environ.*, *115*(8), 1,781–1,800.

Mueller, B., et al. (2011), Evaluation of global observations-based evapotranspiration datasets and IPCC AR4 simulations, *Geophys. Res. Lett.*, *38*, L06402, doi:10.1029/2010GL046230.

Mueller, B., et al. (2013), Benchmark products for land evapotranspiration: LandFlux-EVAL multi-dataset synthesis, *Hydrol. Earth Syst. Sci. Discuss.*, *10*(1), 769–805.

Nasonova, O. N., Y. M. Gusev, and Y. E. Kovalev (2011), Impact of uncertainties in meteorological forcing data and land surface parameters on global estimates of terrestrial water balance components, *Hydrol. Process*, *25*(7), 1,074–1,090.

Nemani, R. R., C. D. Keeling, H. Hashimoto, W. M. Jolly, S. C. Piper, C. J. Tucker, R. B. Myneni, and S. W. Running (2003), Climate-driven increases in global terrestrial net primary production from 1982 to 1999, *Science*, *300*(5625), 1,560–1,563.

New, M., M. Hulme, and P. Jones (2000), Representing twentieth-century space–time climate variability. Part II: Development of 1901–96 monthly grids of terrestrial surface climate, *J. Climate*, *13*(13), 2,217–2,238.

Nicholls, N. (1988), El Niño–Southern Oscillation and rainfall variability, *J. Climate*, *1*(4), 418–421.

Nickl, E., C. J. Willmott, K. Matsuura, and S. M. Robeson (2010), Changes in annual land-surface precipitation over the twentieth and early twenty-first century, *Ann. Assoc. Am. Geogr.*, *100*(4), 729–739.

Oki, T., and S. Kanae (2006), Global hydrological cycles and world water resources, *Science*, *313*(5790), 1,068–1,072.

Peterson, T. C., and R. S. Vose (1997), An overview of the Global Historical Climatology Network temperature database, *Bull. Am. Meteorol. Soc.*, *78*(12), 2,837–2,849.

Poveda, G., A. Jaramillo, M. M. Gil, N. Quiceno, and R. I. Mantilla (2001), Seasonally in ENSO-related precipitation, river discharges, soil moisture, and vegetation index in Colombia, *Water Resour. Res.*, *37*(8), 2,169–2,178.

Priestley, C. H., and R. J. Taylor (1972), Assessment of surface heat-flux and evaporation using large-scale parameters, *Mon. Weather Rev.*, *100*(2), 81–92.

Randall, D. A., et al. (2007), Climate models and their evaluation, in *Climate Change 2007: The Physical Science Basis, Contribution of Working Group I to the Fourth Assessment Report of the Intergovernmental Panel on Climate Change*, edited by S. Solomon et al., pp. 590–662, Cambridge Univ. Press, New York.

Reichle, R. H., R. D. Koster, G. J. M. De Lannoy, B. A. Forman, Q. Liu, S. P. P. Mahanama, and A. Touré (2011), Assessment and enhancement of MERRA land surface hydrology estimates, *J. Climate*, *24*(24), 6,322–6,338.

Rienecker, M. M., et al. (2011), MERRA: NASA's Modern-Era Retrospective Analysis for Research and Applications, *J. Climate*, *24*(14), 3,624–3,648.

Ropelewski, C. F., and M. S. Halpert (1986), North American precipitation and temperature patterns associated with the El Niño/Southern Oscillation (ENSO), *Mon. Weather Rev.*, *114*(12), 2,352–2,362.

Rudolf, B., A. Becker, U. Schneider, A. Meyer-Christoffer, and M. Ziese (2011), New Full Data Reanalysis Version 5 provides high-quality gridded monthly precipitation data, *Global Energy and Water Cycle Experiment (GEWEX) News*, *21*(2), 4–5.

Ryu, Y., et al. (2011), Integration of MODIS land and atmosphere products with a coupled-process model to estimate gross primary productivity and evapotranspiration from 1 km to global scales, *Global Biogeochem. Cycles*, *25*, GB4017, doi:10.1029/2011GB004053.

Sabziparvar, A. A., S. H. Mirmasoudi, H. Tabari, M. J. Nazemosadat, and Z. Maryanaji (2011), ENSO teleconnection impacts on reference evapotranspiration variability in some warm climates of Iran, *Int. J. Climatol.*, *31*(11), 1,710–1,723.

Schlosser, C. A., and X. A. Gao (2010), Assessing evapotranspiration estimates from the Second Global Soil Wetness Project (GSWP-2) simulations, *J. Hydrometeorol.*, *11*(4), 880–897.

Sheffield, J., G. Goteti, and E. F. Wood (2006), Development of a 50-year high-resolution global dataset of meteorological forcings for land surface modeling, *J. Climate*, *19*(13), 3,088–3,111.

Su, Z. (2002), The Surface Energy Balance System (SEBS) for estimation of turbulent heat fluxes, *Hydrol. Earth. Syst. Sci.*, *6*(1), 85–100.

Thornthwaite, C. W., and J. R. Mather (1955), The water balance, in *Publications in Climatology*, pp. 104, Drexel Institute of Technology, New Jersey.

Trenberth, K. E. (2011), Changes in precipitation with climate change, *Climate Res.*, *47*(1-2), 123–138.

Trenberth, K. E., and J. M. Caron (2000), The Southern Oscillation revisited: Sea level pressures, surface temperatures, and precipitation, *J. Climate*, *13*(24), 4,358–4,365.

Trenberth, K. E., and J. T. Fasullo (2009), Global warming due to increasing absorbed solar radiation, *Geophys. Res. Lett.*, *36*, L07706, doi:10.1029/2009GL037527.

Trenberth, K. E., L. Smith, T. T. Qian, A. Dai, and J. Fasullo (2007), Estimates of the global water budget and its annual cycle using observational and model data, *J. Hydrometeorol.*, *8*(4), 758–769.

Twine, T. E., C. J. Kucharik, and J. A. Foley (2005), Effects of El Niño–Southern Oscillation on the climate, water balance, and streamflow of the Mississippi River Basin, *J. Climate*, *18*(22), 4,840–4,861.

Vicente-Serrano, S. M., J. I. López-Moreno, L. Gimeno, R. Nieto, E. Morán-Tejeda, J. Lorenzo-Lacruz, S. Beguería, and C. Azorin-Molina (2011), A multiscalar global evaluation of the impact of ENSO on droughts, *J. Geophys. Res.*, *116*, D20109, doi:10.1029/2011JD016039.

Vimont, D. J., J. M. Wallace, and D. S. Battisti (2003), The Seasonal footprinting mechanism in the Pacific: Implications for ENSO, *J. Climate*, *16*(16), 2,668–2,675.

Vinukollu, R. K., R. Meynadier, J. Sheffield, and E. F. Wood (2011), Multi-model, multi-sensor estimates of global evapotranspiration: Climatology, uncertainties and trends, *Hydrol. Process*, *25*(26), 3,993–4,010.

Wang, K. C., and S. L. Liang (2008), An improved method for estimating global evapotranspiration based on satellite determination of surface net radiation, vegetation index, temperature, and soil moisture, *J. Hydrometeorol.*, *9*(4), 712–727.

Wang, H. J., R. H. Zhang, J. Cole, and F. Chavez (1999), El Niño and the related phenomenon Southern Oscillation (ENSO): The largest signal in interannual climate variation, *Proc. Nat. Acad. Sci.*, *96*(20), 11,071–11,072.

Wang, K., R. E. Dickinson, M. Wild, and S. Liang (2010), Evidence for decadal variation in global terrestrial evapotranspiration between 1982 and 2002: 2. Results, *J. Geophys. Res.*, *115*, D20113, doi:10.1029/2010JD013847.

Wentz, F. J., L. Ricciardulli, K. Hilburn, and C. Mears (2007), How much more rain will global warming bring?, *Science*, *317*(5835), 233–235.

Willmott, C. J., and S. M. Robeson (1995), Climatologically Aided Interpolation (CAI) of terrestrial air temperature, *Int. J. Climatol.*, *15*(2), 221–229.

Willmott, C. J., C. M. Rowe, and W. D. Philpot (1985), Small-scale climate maps: A sensitivity analysis of some common assumptions associated with grid-point interpolation and contouring, *Cartogr. Geogr. Inf. Sci.*, *12*(1), 5–16.

Wolter, K., and M. S. Timlin (1998), Measuring the strength of ENSO events: How does 1997/98 rank?, *Weather*, *53*(9), 315–324.

Yan, H., and H. H. Shugart (2010), An air relative-humidity-based evapotranspiration model from eddy covariance data, *J. Geophys. Res.*, *115*, D16106, doi:10.1029/2009JD013598.

Yan, H., et al. (2012), Global estimation of evapotranspiration using a leaf area index-based surface energy and water balance model, *Remote Sens. Environ.*, *124*, 581–595.

Yang, X., and T. DelSole (2011), Systematic comparison of ENSO teleconnection patterns between models and observations, *J. Climate*, *25*(2), 425–446.

Zeng, Z. Z., S. L. Piao, X. Lin, G. D. Yin, S. S. Peng, P. Ciais, and R. B. Myneni (2012), Global evapotranspiration over the past three decades: Estimation based on the water balance equation combined with empirical models, *Environ. Res. Lett.*, *7*(1), doi:10.1088/1748-9326/7/1/014026.

Zhang, K., J. S. Kimball, R. R. Nemani, and S. W. Running (2010), A continuous satellite-derived global record of land surface evapotranspiration from 1983 to 2006, *Water Resour. Res.*, *46*, W09522, doi:10.1029/2009WR008800.

Zhu, Z., J. Bi, Y. Pan, S. Ganguly, A. Anav, L. Xu, A. Samanta, S. Piao, R. Nemani, and R. Myneni (2013), Global data sets of vegetation leaf area index (LAI)3g and fraction of photosynthetically active radiation (FPAR) 3g derived from Global Inventory Modeling and Mapping Studies (GIMMS) normalized difference vegetation index (NDVI3g) for the period 1981 to 2011, *Remote Sensing*, *5*(2), 927–948.